The Astrophysical Journal, 703:1778–1790, 2009 October 1 doi:10.1088/0004-637X/703/2/1778

SPECTROSCOPIC IDENTIFICATIONS OF *SPITZER* SOURCES IN THE SWIRE/*XMM-NEWTON*/ELAIS-S1 FIELD: A LARGE FRACTION OF ACTIVE GALACTIC NUCLEI WITH HIGH $F(24\ \mu\mathrm{m})/F(R)$ RATIO

N. Sacchi[1,2], F. La Franca[1], C. Feruglio[3,4], F. Fiore[3], S. Puccetti[5], F. Cocchia[3], S. Berta[6], M. Brusa[6], A. Cimatti[7], A. Comastri[8], A. Franceschini[9], C. Gruppioni[8], R. Maiolino[3], I. Matute[1,10], M. Polletta[11], L. Pozzetti[8], F. Pozzi[7], C. Vignali[7], G. Zamorani[8], S. Oliver[12], M. Rowan-Robinson[13], G. Smith[14], and C. Lonsdale[15]

[1] Dipartimento di Fisica, Università Roma Tre, via della Vasca Navale 84, I-00146 Roma, Italy; sacchi@fis.uniroma3.it, lafranca@fis.uniroma3.it
[2] TNG Fundación Galileo Galilei-INAF, Rambla José Ana Fernández Pérez 7, 38712 Breña Baja, TF, Spain
[3] INAF-Osservatorio Astronomico di Roma, via Frascati 33, I-00040, Monteporzio Catone, Italy
[4] CEA, Irfu, Service d'Astrophysique, Centre de Saclay, F-91191 Gif-sur-Yvette, France
[5] ASI Science Data Center, via G. Galilei, I-00044 Frascati, Italy
[6] Max Planck Institut für Extraterrestrische Physik, Giessenbachstrasse 1, D-85748 Garching, Germany
[7] Dipartimento di Astronomia, Università di Bologna, via Ranzani 1, I-40127 Bologna, Italy
[8] INAF-Osservatorio Astronomico di Bologna, via Ranzani 1, I-40127 Bologna, Italy
[9] Dipartimento di Astronomia, Università di Padova, vicolo dell'Osservatorio 2, I-35122 Padova, Italy
[10] INAF-Osservatorio Astronomico di Arcetri, largo E. Fermi 5, I-50125 Firenze, Italy
[11] INAF-IASF Milano, via E. Bassini 15, I-20133 Milano, Italy
[12] Astronomy Centre, Department of Physics and Astronomy, University of Sussex, Falmer, Brighton BN1 9QJ, UK
[13] Astrophysics Group, Blackett Laboratory, Imperial College of Science Technology and Medicine, Prince Consort Road, London SW7 2BZ, UK
[14] Center for Astrophysics and Space Sciences, University of California, San Diego, La Jolla, CA 92093-0424, USA
[15] Infrared Processing and Analysis Center, California Institute of Technology 100-22, Pasadena, CA 91125, USA
Received 2008 November 16; accepted 2009 July 23; published 2009 September 14

ABSTRACT

We present a catalog of optical spectroscopic identifications of sources detected by *Spitzer* at 3.6 or 24 μm down to $\sim$10 and $\sim$280 μJy, respectively, in the SWIRE/*XMM-Newton*/ELAIS-S1 field and classified via line width analysis and diagnostic diagrams. A total of 1376 sources down to $R \sim 24.2$ mag have been identified (1362 detected at 3.6 μm, 419 at 24 μm, and 405 at both) by low-resolution optical spectroscopy carried out with FORS2, VIMOS, and EFOSC2 at the Very Large Telescope and 3.6 m ESO telescope. The spectroscopic campaigns have been carried out over the central 0.6 deg^2 area of ELAIS-S1 which, in particular, has also been observed by *XMM-Newton* and *Chandra*. We find the first direct optical spectroscopic evidence that the fraction of active galactic nuclei (AGNs; mostly AGN2) increases with increasing $F(24\ \mu\mathrm{m})/F(R)$ ratio, reaching values of 70($\pm$20)% in the range $316 < F(24\ \mu\mathrm{m})/F(R) < 1000$. We present an Infrared Array Camera–Multiband Imaging Photometer color–color diagram able to separate AGN1 from obscured AGN2 candidates. After having corrected for the spectroscopic incompleteness of our sample, the result is that the AGN fraction at $F(24\ \mu\mathrm{m})$ $\sim$0.8 mJy is $\sim$22($\pm$7)% and decreases slowly to $\sim$19($\pm$5)% down to $F(24\ \mu\mathrm{m}) \sim 0.3$ mJy.

Key words: galaxies: active – infrared: galaxies – surveys

Online-only material: color figures, machine-readable table

1. INTRODUCTION

Multi-wavelength surveys are fundamental instruments to study the cosmological evolution of extragalactic sources. Each region of the electromagnetic spectrum provides information on different physical mechanisms which take place in the galaxies. The emission in the mid-infrared (MIR) band is mainly produced by dust heated either by the stars (particularly during periods of strong star formation activity) or by the emission originating in an active galactic nucleus (AGN). In several cases, both causes contribute to the formation of the total spectral energy distribution (SED) in the MIR (see, e.g., Polletta et al. 2008; Donley et al. 2008 and references therein).

In recent years, *XMM-Newton*- and *Chandra*-based X-ray surveys have been able to delineate the density and evolution of X-ray unabsorbed and even moderately absorbed AGNs (Compton-thin; $N_H = 10^{22}$–10^{24} cm^{-2}) up to redshift $\sim$4 (see, e.g., Ueda et al. 2003; La Franca et al. 2005). The fraction of absorbed AGNs is observed to decrease with increasing luminosity (e.g., Ueda et al. 2003; La Franca et al. 2005; Hasinger 2008; see also Lawrence & Elvis 1982) and to increase with increasing redshift (La Franca et al. 2005; Ballantyne et al. 2006; Treister & Urry 2006; Hasinger 2008; Treister et al. 2009). In this framework, in order to reproduce the cosmic X-ray background, a population of heavily X-ray absorbed AGNs (Compton-thick; CT) as numerous as the Compton-thin one is expected. Because of the strong X-ray absorption, these CT AGNs are difficult to select even in the X-ray band.

As the AGN (absorbed) activity is expected to contribute significantly to the MIR SED, observations in the MIR regime are potentially useful for selecting AGNs, including those which are undetected in the X-ray band.

The launch of the *Spitzer* telescope has allowed the construction of several large area multi-wavelength databases with MIR coverage, such as (for example) the 9 deg^2 NOAO Deep Wide-Field Survey (NDWFS) of the Boötes field (Murray et al. 2005), the 3.7 deg^2 Extragalactic First Look Survey (E-FLS; Fadda et al. 2006) and the smaller 0.5 deg^2 of the All-Wavelength Extended Groth Strip International Survey (AEGIS; Davis et al. 2007). Indeed, the use of *Spitzer* colors has been revealed to be efficient (if not complete) in selecting AGNs (e.g., Lacy et al. 2004, 2007; Stern et al. 2005). Using both *Spitzer* and X-ray observations, Brand et al. (2006), Treister et al. (2006), and Donley et al. (2008) have evaluated the fraction of AGNs as a function

of the 24 μm flux, which results in being around 30%–45% at ~3 mJy, decreasing to about 10% at ~0.4 mJy.

Many studies have shown evidence of the existence of X-ray absorbed (Compton-thick) *Spitzer*-selected AGNs (e.g., Donley et al. 2005, 2007; Alonso-Herrero et al. 2006; Polletta et al. 2006; Steffen et al. 2007; Alexander et al. 2008). Maybe the most efficient criterion in selecting X-ray-absorbed AGNs is based on selecting sources with large $F(24\ \mu m)/F(R)$ ratios, in some cases linked to radio observations (e.g., Martínez-Sansigre et al. 2005, 2007). Because of the faint optical fluxes these sources are difficult to spectroscopically identify in the optical, and, in fact, the AGN classifications for this class of objects are mainly based on MIR spectroscopy with the Infrared Spectrograph (IRS) on board *Spitzer* (e.g., Houck et al. 2005; Weedman et al. 2006; Yan et al. 2007; Brand et al. 2008). Because of the low resolution of the IRS spectra, for many sources the classification and the redshift measure are derived from the identification of the 9.7 μm silicate absorption features on approximate power-law spectral shapes.

Using stacked *Chandra* images of sources with large $F(24\ \mu m)/F(R)$ ratios, Daddi et al. (2007) and Fiore et al. (2008, 2009) have shown that the *average* X-ray spectrum can be reproduced if a high percentage (~80%) of the sources in the sample are highly X-ray absorbed (even Compton-thick) AGNs (but see Donley et al. 2008 and Pope et al. 2008 for partly different conclusions). This result is itself important for the understanding of AGN density evolution, but it needs to be complemented with a quantification of the real fraction of AGNs among these sources. In fact, the above studies are mainly based on photometric redshifts and lack direct optical spectroscopic identifications and classifications. Such measurements are crucial in order to understand how much of the average resulting hard X-ray spectrum is diluted and/or contaminated by starburst galaxies included in the samples (see, e.g., Polletta et al. 2008; Donley et al. 2008).

Brand et al. (2007) have studied in the near IR the spectrum of 10 ULIRG sources with 24 μm fluxes larger than 0.8 mJy and large $F(24\ \mu m)/F(R)$ ratios and found that the SEDs were compatible with a mixed contribution of AGN and starburst activity. Studying the SED and MIR spectrum of 21 obscured AGNs with large $F(24\ \mu m)/F(R)$ ratios, and 24 μm fluxes larger than 1 mJy, Polletta et al. (2008) found that the contribution by the starburst component to the bolometric luminosity was below 20%.

Dey et al. (2008) have measured spectroscopic redshift for 86 very luminous dust-obscured galaxies with $F(24\ \mu m) > 0.3$ mJy and $F(24\ \mu m)/F(R) > 1000$ in the Boötes field, and find a broad redshift distribution centered at $z \sim 2$. Roughly half the redshifts are the results of *Spitzer* IRS observations, and half come from ground-based optical or NIR spectroscopy. However, no optical spectral classification of the galaxies has been discussed in their work.

Here we present the optical spectroscopic identifications and classification of 1376 sources of the central 0.6 deg^2 of the ELAIS-S1 field included in the *Spitzer* Wide-area Infrared Extragalactic Survey (SWIRE; Lonsdale et al. 2003, 2004) and then use our database to estimate the fraction of AGNs as a function of the MIR flux and the $F(24\ \mu m)/F(R)$ ratio.

Throughout this work with "fraction of AGN," we mean the fraction of extragalactic sources in which is possible to reveal, via optical line width analysis and diagnostic diagrams (see, e.g., Veilleux & Osterbrock 1987; Kewley et al. 2006), the presence of an active nucleus, regardless of its strength relative to the host galaxy. In the case of uncertain AGN signatures, we adopted a conservative approach. Our database allows the first direct estimate (using optical spectra) of the fraction of AGNs among the sources with large (>316) $F(24\ \mu m)/F(R)$ ratios.

We adopt a flat cosmology with $H_0 = 70$ km s^{-1} Mpc^{-1}, $\Omega_M = 0.30$, and $\Omega_\Lambda = 0.70$. Magnitudes are given in the Vega system. Unless otherwise stated, uncertainties are quoted at the 68% (1σ) confidence level.

2. MULTI-WAVELENGTH DATABASE

The ELAIS-S1 field (center: $\alpha = 00^h35^m00\overset{s}{.}0$, $\delta = -43^\circ30'00''$; J2000) is part of the SWIRE survey (Lonsdale et al. 2004) which is the largest *Spitzer* Legacy Program. SWIRE includes six high-latitude fields, totaling 49 deg^2 (~7 of which on the ELAIS-S1 region) observed by *Spitzer* in four bands (3.6, 4.5, 5.8, and 8.0 μm) with the Infrared Array Camera (IRAC; Fazio et al. 2004), and in three bands (24, 70, and 160 μm) with the Multiband Imaging Photometer (MIPS; Rieke et al. 2004).

Originally, the ELAIS-S1 field was selected as one of the four fields of the European Large Area *ISO* Survey (ELAIS) covering a total of 12 deg^2 at 15 μm (Oliver et al. 2000; Rowan-Robinson et al. 2004). The size of the ELAIS-S1 field is 4 deg^2 and the 15 μm catalog published by Lari et al. (2001) contains 329 extragalactic sources over the flux range 0.5–100 mJy. The imaging and spectroscopic identification and classification of the 15 μm sources have been presented by La Franca et al. (2004; see also La Franca et al. 2007 and Gruppioni et al. 2008).

An area of 3.9 deg^2 is covered by radio observations obtained with Australian Telescope Compact Array (ATCA) down to $S_{1.4-GHz} \simeq 30$ μJy (1σ; Middelberg et al. 2008; see also Gruppioni et al. 1999). ELAIS-S1 is also one of the targets selected by the *GALEX* Deep Survey, which has deeply covered the central part of S1 in the far- and near-UV (Burgarella et al. 2005).

2.1. Spitzer Data

The *Spitzer*/SWIRE observations in ELAIS-S1 cover a ~7 deg^2 region larger than the whole 4 deg^2 *ISO* region, in all the IRAC and MIPS bands, reaching 5σ sensitivities of 3.7, 5.4, 48, 37.8, 230, 18×10^3, and 150×10^3 μJy in the 3.6, 4.5, 5.8, 8.0, 24, 70, and 160 μm channels, respectively (Lonsdale et al. 2004). The SWIRE data in ELAIS-S1 have been released to the community in autumn 2005 (Data Release 3, DR3) through the query building GATOR at the NASA/Infrared Science Archive.[16] However, for the purposes of this work, we had access to the SWIRE working catalogs, which contain all of the sources in the public catalog, but reach deeper flux densities (on average about a factor of 30% fainter). Details about the SWIRE data reduction, that was carried out by the Spitzer Science Center and SWIRE team, can be found in the Data Release paper (Surace et al. 2005). Details on the generation of the *Spitzer* band merged catalog can be found in Gruppioni et al. (2008).

While the original SWIRE/ELAIS-S1 field is ~7 deg^2, here we concentrate on a central rectangular area, of 0.6 deg^2, with limits $8\overset{\circ}{.}21 < \alpha < 9\overset{\circ}{.}245$ and $-43\overset{\circ}{.}91 < \delta < -43\overset{\circ}{.}116$ nearly including the four *XMM-Newton* observations of the area described by Puccetti et al. (2006; see Figure 1). This area contains a total of 35,021 sources detected by *Spitzer*, 32,815 at 3.6 μm and 2056 at 24 μm (1920 have been detected in both bands). Because of their bright flux limits, we excluded from the catalog the MIPS measures at 70 and 160 μm.

[16] http://irsa.ipac.caltech.edu/applications/Gator/

Table 1
Number of Good-Quality[a] Spectra

Period	Instrument	Total	3.6 μm	24 μm	X&24 μm
...	15 μm Catal.[b]	60	54	59	8
73-04	VIMOS	888	885	139	35
75-05	VIMOS	328	327	129	18
76-05	EFOSC2	20	19	12	3
77-06	FORS2-SLIT	11	11	11	6
78-06	FORS2-MOS	69	66	69	13
Total	...	1376	1362	419	83

Notes.
[a] We define as "good quality" those spectra with quality flag $\geqslant$1.5 (see Section 3.5).
[b] La Franca et al. (2004, 2007).

2.2. Optical and NIR Data

B, *V*, and *R* images, down to $B \sim 25$, $V \sim 25$, and $R \sim 24.5$ (95% completeness) have been obtained with the WFI at the ESO 2.2 m telescope within the framework of the ESO-*Spitzer* wide-area Imaging Survey (ESIS; Berta et al. 2006; PI: Alberto Franceschini), while about 1 deg^2 of ELAIS-S1 has been covered by deep K' and *J* bands exposures with SOFI at the ESO NTT telescope (I. Matute et al. 2010, in preparation). Recently, *I*- and *z*-band photometry, down to $I \sim 23$ and $z \sim 22.5$ (90% completeness), carried out with VIMOS at the Very Large Telescope (VLT), has been released (Berta et al. 2008).

2.3. X-ray Band Data

The first very shallow ($\sim 10^{-13}$ cgs; 2–10 keV) X-ray band observations on the ELAIS-S1 area were carried out with *BeppoSAX* and presented by Alexander et al. (2001). More recently, the central $\sim$0.6 deg^2 region of ELAIS-S1 has been surveyed in the X-ray band with *XMM-Newton* (four pointings of about 70 "useful" ks each) with 478 sources detected, 395 in the soft (0.5–2 keV) band down to a flux of 5.5×10^{-16} cgs and 205 in the hard (2–10 keV) band down to a flux of 2×10^{-15} cgs (Puccetti et al. 2006).

The regions with the highest *XMM-Newton* sensitivity ($\sim$65% of the full *XMM-Newton* area) were later target of 165 ks *Chandra* observations, reaching on-axis sensitivities of 2×10^{-15} cgs (2–10 keV; S. Puccetti et al. 2010, in preparation), with the aim of obtaining precise positions for the X-ray sources.

3. OPTICAL SPECTROSCOPY

ELAIS-S1 was the target of several spectroscopic campaigns with ESO telescopes. The follow-up programs of the 15 μm ELAIS-S1 sources provided 60 identifications of $R < 22$ sources within our investigated area (La Franca et al. 2004, 2007). In the period 2004–2006, five follow-up programs were accepted, with the aim of obtaining spectroscopic identifications for the *XMM-Newton*, 3.6 and 24 μm sources in the SWIRE/*XMM-Newton*/ELAIS-S1 area. The number of spectra obtained in each spectroscopic run is shown in Table 1.

3.1. VIMOS Observations

Spectroscopic targets with a limiting magnitude of $R \sim 24$ were observed with the VIsible MultiObject Spectrograph (VIMOS) at the VLT in multi-object spectroscopy (MOS) mode, with the Low-Resolution Red (LRR) grism ($\lambda/\Delta\lambda \sim 210$), covering the 5500–9500 Å wavelength range, with 1–4 hr exposure time per pointing, totaling 66 hr of observing time. VIMOS data reduction was carried out using the VIMOS Interactive Pipeline and Graphical Interface (VIPGI) developed by INAF Milano (Scodeggio et al. 2005). Two observing runs were carried out in the years 2004 and 2005. The first observing run was dedicated to identifying *K*-band and X-ray sources located in the western half of the area, as the SWIRE catalog was not yet available. The second run (as all the following runs) was dedicated to observing 24 μm and X-ray sources, while the 3.6 μm sources were used as fillers of the masks. The observations were carried out in the eastern half of the area, but unfortunately it was not possible to observe the southeastern corner (see Figure 1). In total 1473 spectra were collected: 1212 of good quality (quality flag $\geqslant$1.5; see Section 3.5 for a description of the quality flag).

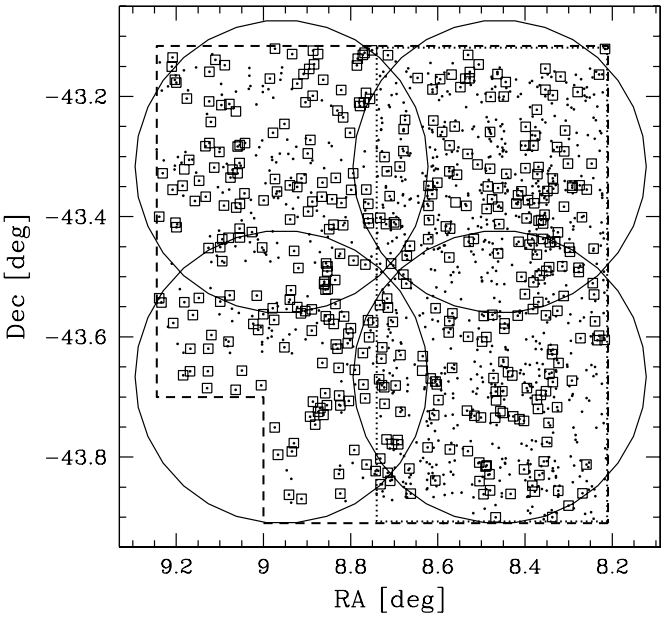

Figure 1. Position on sky of 3.6 μm (dots) and 24 μm (open squares) detected sources with a reliable redshift estimate. The circles indicate the area covered by the four *XMM-Newton* pointings. The dashed and dotted lines show the statistically useful areas of the 24 μm and 3.6 μm spectroscopic samples, respectively (see Section 3.1).

3.2. EFOSC2 and FORS2 (Long Slit) Observations

Four nights of visiting-mode observation in single-slit mode with EFOSC2 at the ESO-3.6 m in La Silla allowed us to observe 20 optically bright ($R < 20$) targets in the 4000–9000 Å wavelength range with grisms 6 and 13.

Twenty hours of observing time was allocated with FORS2 at the VLT in long-slit mode. A total of 12 good-quality spectra were obtained with the 150*I* grism ($\lambda/\Delta\lambda \sim 260$), covering the wavelength range 3700–10300 Å.

3.3. FORS2 (MOS) Observations

Spectroscopy of 69 faint sources has been carried out with FORS2 at the VLT in 2006 in MOS (MOvable-Slit) mode, with 2.5 hr exposure times per pointing, corresponding to a total of 28 hr of observing time. The same grism setup of the FORS2 Long-Slit observations was used (see the previous section).

3.4. Data Reduction

The reduction process used standard MIDAS and IRAF facilities, except for VIMOS data which required a specific

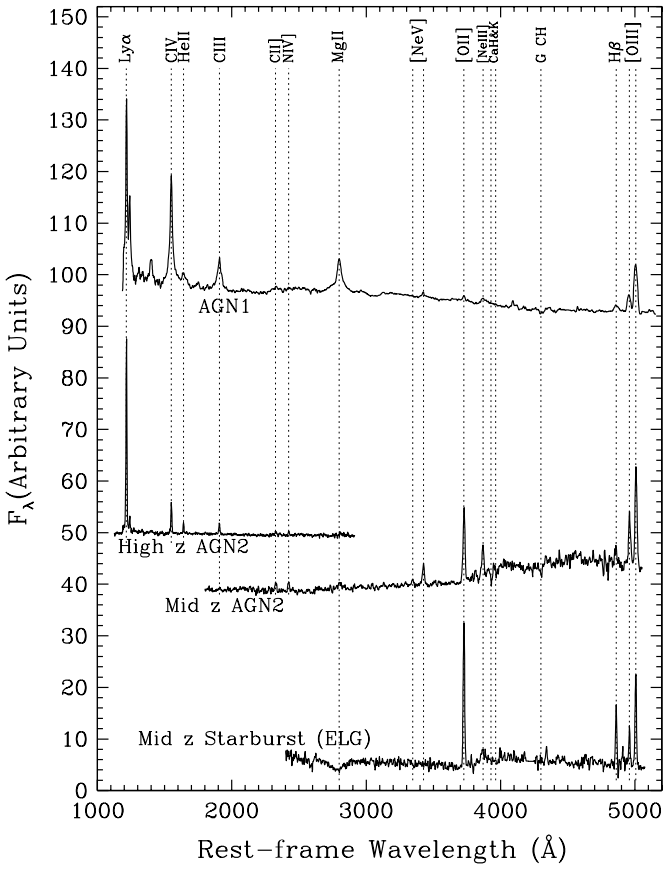

Figure 2. Composite spectra of 25 AGN1 ($1 < z < 3$), 7 high ($1.6 < z < 2.6$) and 12 middle ($0.8 < z < 1.2$) redshift AGN2, and 20 ELG ($0.6 < z < 1.2$).

software package (VIPGI; Scodeggio et al. 2005). The raw data were bias-subtracted, corrected for pixel-to-pixel variations (flat field), and eventually sky-subtracted. Wavelength calibrations were carried out by comparison with exposures of He and Ar lamps. Relative flux calibration was carried out by observations of several spectrophotometric standard stars.

3.5. Classification

Spectroscopic redshifts were obtained using both the `rvidlines` IRAF tool and an instrument-optimized MIDAS procedure, which allowed to compute the average of the redshifts corresponding to each measured line center. We assigned a quality flag to each redshift: [2] for the determinations based on at least two confirmed features (typically 3–4 or more absorption/emission lines besides the continuum shape); [1.5] for two very plausible features (besides the continuum shape); and [1] for one clearly recognizable feature, [0.5] for tentative estimates of redshift. The spectroscopic catalogs we present include only highly reliable redshift estimates, with quality flag $\geqslant$ [1.5].

We classified the sources according to their optical spectral features in five broad classes.

1. Broad-line AGN (AGN1): type-1 AGN with broad (FWHM > 2000 km s^{-1}) emission lines such as C IV λ1549, C III] λ1909, Mg II λ2798, Hβ, Hα. As a reference, in Figure 2, the composite spectrum of a sub-sample of 25 ($1 < z < 3$)[17] type-1 AGNs is shown.
2. Narrow-line AGN (AGN2): type-2 AGN with narrow (FWHM < 2000 km s^{-1}) high-ionization emission lines (C IV λ1549, C III] λ1909, [Ne V] λ3426) or low-ionization ([O II] λ3727, Hβ, [O III] λλ5007, 4959, Hα, [S II] λ6725) emission lines with flux ratios indicating the presence of an AGN (e.g., Osterbrock 1989; Veilleux & Osterbrock 1987; Tresse et al. 1996). In Figure 2, the composite spectra of seven high ($1.6 < z < 2.6$) and 12 middle ($0.8 < z < 1.2$) redshift[2] AGN2s are shown.
3. Emission-line galaxies (ELGs): sources with narrow emission lines, but no clear AGN signature in the optical spectra (see Figure 2). They show strong low-ionization emission lines that may be produced by thermal photons from hot stars. They often show also CaHK λλ3933, 3969 absorption and the continuum break at 4000 Å. This class is likely to include a fraction of NL AGNs, possibly misclassified due to a small wavelength range (e.g., only [O II] λ3727 visible), low signal-to-noise ratio (S/N) spectra, or dilution by the host galaxy emission. In Figure 2, the composite spectrum of 20 middle ($0.6 < z < 1.2$) redshift[2] ELGs is shown.
4. Absorption-line galaxies (GALs): sources with spectra typical of early-type galaxies, characterized by absorption features such as CaHK λλ3933, 3969 and strong 4000 Å continuum break.
5. Stars: sources with stellar spectra (mainly of cold M-stars), characterized by a blackbody continuum and absorption features.

The wavelength range of our spectra (mostly in the interval 4500–9500 Å), is wide enough to classify the sources. In the case of those narrow lines sources, where only the region of the [O II] λ3727 line was visible, we used the presence (or not) of the high-ionization [Ne V] λ3426 line to discriminate between AGN2s and ELGs. In any case, the AGN2 classification has been conservatively assigned only in fully reliable conditions. Because of the presence of broad emission lines in their spectra, even in the case of low S/N data, we can exclude that type-1 AGNs have been wrongly classified as either AGN2 or ELG.

As far as the galaxies with no emission lines (passive) are concerned, we were not able to measure redshifts larger than one (with calcium-break redshifted out of the wavelength coverage). However, this bias should be small in the 24 μm sample, as the fraction of energy emitted in the MIR by the passive galaxies is smaller than in the other galaxies (see, e.g., the SED library shown in Figure 1 of Polletta et al. 2007), and therefore the 24 μm sample should be scarcely populated by no emission line galaxies (see discussion in Section 4.1). This bias could instead affect the 3.6 μm sample[18] which, however, has not been scientifically used in this work.

4. THE SPECTROSCOPIC CATALOG

In Table 2, we present the whole spectroscopic catalog consisting of 1376 optical counterparts of 3.6 and 24 μm *Spitzer* sources (whose redshift estimates have a quality flag $\geqslant$ [1.5]). For every source we report: the ESIS catalog identification code (from Berta et al. 2006), sky coordinates in degree units (J2000) of the optical counterpart and its *R*-band magnitude, redshift, redshift quality code (only sources with 1.5 or 2.0 redshift quality are included), spectroscopic classification code ([1] =

[17] These redshift and wavelength intervals were chosen in order to maximize the number of overlapping spectra.

[18] Where indeed we found a fraction of classified no emission line galaxies four times larger than in the 24 μm sample; see discussion in Section 4.2.

Table 2
The Spectroscopic Catalog

ID_{ESIS}	R.A. (deg)	Decl. (deg)	R (mag)	z	q	cls	ID_{SWIRE}	$S_{3.6\,\mu m}$ (log(μJy))	$S_{24\,\mu m}$ (log(μJy))	ID_X
(1)	(2)	(3)	(4)	(5)	(6)	(7)	(8)	(9)	(10)	(11)
J003522.49−432517.45	8.84371	−43.42152	18.65	0.225	2.0	4	SWIRE3_J003522.50−432517.3	2.2335	···	311
J003521.34−432509.51	8.83894	−43.41928	21.71	0.636	2.0	2	SWIRE3_J003521.36−432509.3	1.7075	···	301
J003453.39−431802.46	8.72240	−43.30064	20.65	1.075	2.0	1	SWIRE3_J003453.39−431802.1	1.8465	2.5470	258
J003443.36−431713.39	8.68062	−43.28707	18.42	0.000	2.0	5	SWIRE3_J003443.36−431713.3	2.7933	···	245
J003407.39−430751.01	8.53081	−43.13084	18.91	0.188	2.0	2	SWIRE3_J003407.41−430750.9	2.2723	2.1869	185
J003424.30−432037.21	8.60127	−43.34372	21.47	1.041	2.0	1	SWIRE3_J003424.32−432037.2	1.5117	2.5663	216
J003429.29−432409.80	8.62204	−43.40269	21.28	1.065	2.0	1	SWIRE3_J003429.30−432409.5	1.7462	···	229
J003416.03−433338.06	8.56669	−43.56065	22.17	0.956	2.0	1	SWIRE3_J003416.02−433338.2	1.6669	2.5285	205
J003320.65−433716.86	8.33610	−43.62132	19.48	0.287	2.0	2	SWIRE3_J003320.68−433716.6	2.1074	2.4607	80
J003503.93−432847.13	8.76638	−43.47975	20.78	1.108	2.0	1	SWIRE3_J003503.94−432846.9	2.2380	2.8999	270
J003716.73−434151.12	9.31958	−43.69757	17.91	0.226	2.0	3	SWIRE3_J003716.71−434151.1	2.5961	3.3699	···
J003546.69−430340.11	8.94461	−43.06111	17.30	0.147	2.0	3	SWIRE3_J003546.72−430339.8	2.8383	3.4389	···
J003635.09−430133.70	9.14621	−43.02603	17.61	0.208	2.0	3	SWIRE3_J003635.10−430133.6	2.7766	3.4651	···
J003531.00−430117.55	8.87917	−43.02154	17.14	0.146	2.0	3	SWIRE3_J003531.01−430117.4	2.7604	3.3664	···

Notes. Column 1: ESIS identification name from Berta et al. (2006). Columns 2 and 3: coordinates (J2000). Column 4: *R*-band Vega magnitude. Column 5: redshift. Column 6: redshift quality code: [2.0] = reliable, based on >2 confirmed lines; [1.5] = very plausible, based on two lines. Column 7: spectroscopic classification code: [1] = type-1 AGN; [2] = type-2 AGN; [3] = ELG; [4] = normal galaxy; [5] = star. Column 8: SWIRE identification name of the most probable corresponding *Spitzer* source. Column 9: flux at 3.6 μm. Column 10: flux at 24 μm. Column 11: *XMM-Newton* source name, see Feruglio et al. (2008).

(This table is available in its entirety in a machine-readable form in the online journal. A portion is shown here for guidance regarding its form and content.)

type-1 AGN; [2] = type-2 AGN; [3] = ELG; [4] = normal galaxy; [5] = star). We report also the SWIRE identification code and the 3.6 and 24 μm flux densities, in log[μJy] units, of the corresponding *Spitzer* sources. For those sources detected in the X-rays, the ID code from the catalog of Feruglio et al. (2008) is also reported.

The spectroscopic sample of the (both *Spitzer* detected and not) *XMM-Newton* sources has been presented in a separate publication by Feruglio et al. (2008). Therefore, the spectroscopic identification of any X-ray detected *Spitzer* source appears in both catalogs.

4.1. The 24 μm Sample

Because of the incomplete execution of the second VIMOS run, the statistically useful area of the field for spectroscopic identifications of the 24 μm sources is a rectangle with limits $8\overset{\circ}{.}21 < \alpha < 9\overset{\circ}{.}245$ and $-43\overset{\circ}{.}91 < \delta < -43\overset{\circ}{.}116$, where all sources having $\alpha > 9\overset{\circ}{.}0$ and $\delta < -43\overset{\circ}{.}7$ have been excluded (see Figure 1).

A total of 1932 24 μm sources were detected by *Spitzer* within this 0.56 deg^2 studied area, 1512 of which (78%) have been identified in the *R*-band optical ESIS catalog. Four hundred and nineteen sources have been spectroscopically identified: 399 result to be extragalactic sources and 20 stars. The extragalactic sources were classified into 107 AGNs (27.3%, 52 AGN1s and 57 AGN2s), 253 ELGs (63.4%), and 37 GALs (9.3%). Figure 3 shows the histogram of the 24 μm flux of all sources (top line), those with an *R*-band detection (hatched region) and those with a reliable redshift estimate (darker shaded area).

In Figure 4, the distribution of the *R* magnitude as a function of the 24 μm flux is shown, with the indication of the spectroscopically identified and the X-ray detected sources. The fraction of spectroscopically identified sources decreases at both faint optical and 24 μm fluxes. This trends should be taken into account when these data are used. In our analyses (see Section 5), we selected a sub-sample with 24 μm fluxes brighter than 280 μJy and magnitudes brighter than $R = 24.2$, which corresponds to the largest possible sample where sufficient spectroscopic information exists (at these flux limits the fraction of spectroscopically identified sources is about 10%).

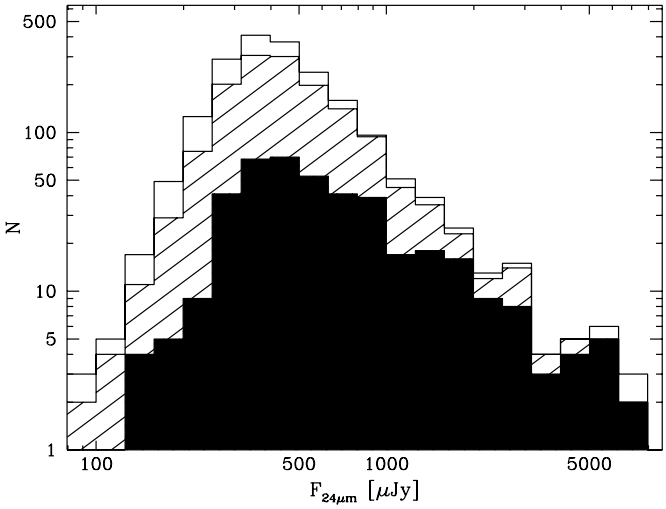

Figure 3. 24 μm flux density distribution of all *Spitzer* sources (line on top), those with an *R*-band detection (hatched region) and those with a reliable redshift estimate (darker shaded area).

We have compared the spectroscopic sample (including only sources with a reliable redshift identification; see the previous section) with the "parent" 24 μm sample. In the upper left panel of Figure 5, the fraction of the 24 μm sources brighter than $R = 24$ mag which have been detected at 3.6 μm as a function of the 24 μm flux is shown. At 24 μm fluxes brighter than 280 μJy (once the uncertainties are taken into account), no significant difference is found between the spectroscopic sample and the parent 24 μm sample: in both samples, in any bin more than 95% of the sources brighter than $R = 24$ have been detected at 3.6 μm. No significant difference is found, either, between the two samples, in the value of the $F(24\,\mu m)/$

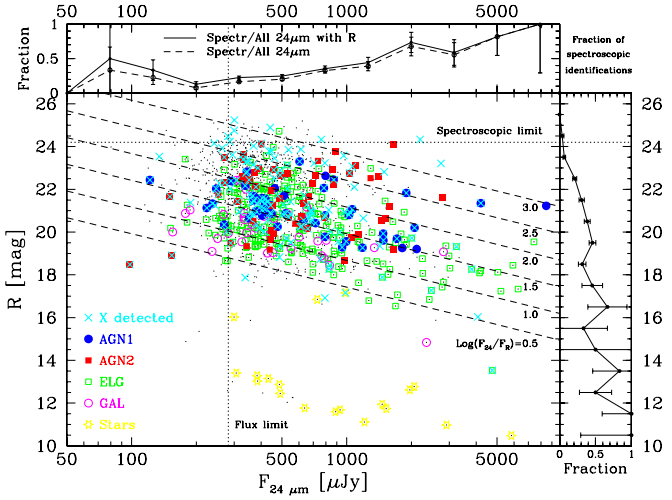

Figure 4. Central: R magnitude as a function of the 24 μm flux. Those having a reliable redshift estimate are represented by symbols whose meaning is shown in the legend. Sources detected in the X-ray are represented by cyan crosses. The dashed lines indicate the loci with equal $F(24\ \mu m)/F(R)$ ratio (whose values are reported in the labels). The vertical dotted line represents the 24 μm flux limit of 280 μm used to measure the fraction of AGNs, while the horizontal dotted line represents the $R = 24.2$ mag limit of the spectroscopic identifications. Upper: fraction of the spectroscopically identified sources as a function of the 24 μm flux for the whole 24 μm sample (dashed line) and the R-band detected 24 μm sample (continuous line). Right: fraction of the spectroscopically identified 24 μm sources as a function of the R-band magnitude.

(A color version of this figure is available in the online journal.)

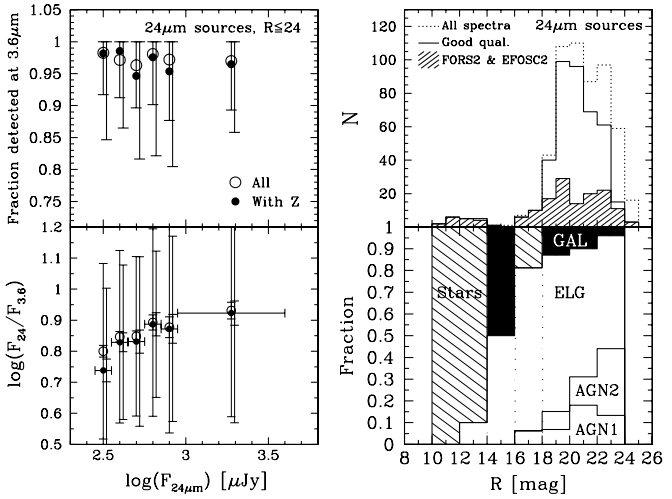

Figure 5. Upper left: fraction of the 24 μm sources brighter than $R = 24$ which have been detected at 3.6 μm as a function of the 24 μm flux. The whole sample and the spectroscopically identified one are represented by open and filled circles, respectively. Lower left: ratio of the 24 μm and 3.6 μm flux densities as a function of the 24 μm flux for the same samples. Symbols are as in the previous panel. Thick vertical error bars correspond to the (1σ) uncertainties on the mean, while the light vertical error bars show the (1σ) spread of the distributions. Upper right: R magnitude distribution of the spectroscopically observed 24 μm sources. The dotted line is the distribution of all the spectra, while the continuous line is the distribution of the "good-quality" (qual $\geqslant$ 1.5) spectra presented in this work. The shaded area is the histogram of those sources whose spectra have been mainly obtained with FORS2/VLT (some of the brightest with EFOSC2/3.6 m or DFOSC). Lower right: fraction of the "good-quality" (qual $\geqslant$ 1.5) spectra of the 24 μm sources according to the spectroscopic class. Each histogram includes the classes below itself.

$F(3.6\ \mu m)$ ratio as a function of the 24 μm flux (see the lower left panel in Figure 5). We can then affirm that, although the fraction of spectroscopically identified sources depend either from the optical and 24 μm fluxes, the average MIR SED properties

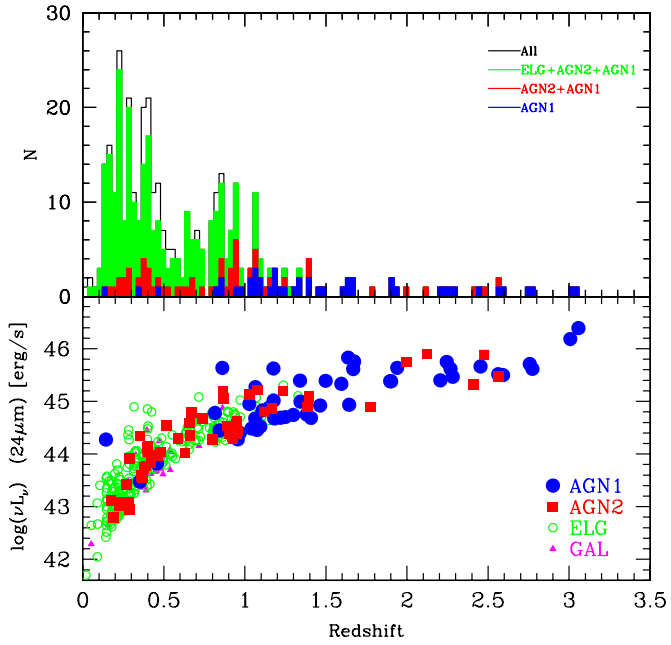

Figure 6. Top: redshift distribution of all 24 μm detected *Spitzer* sources. Those spectroscopically classified as AGN1, AGN2, and ELG are indicated in blue, red, and green colors, respectively. Bottom: $\log(\nu L_\nu)$ 24 μm luminosity–redshift diagram of all spectroscopically identified 24 μm sources. Blue circles, red squares, and green circles represent AGN1, AGN2, and ELG, respectively.

(A color version of this figure is available in the online journal.)

of the spectroscopically identified sources are not significantly different from those of the parent 24 μm sample (with R brighter than 24 mag).

In the upper right panel of Figure 5, the R-band distribution of the spectroscopically identified 24 μm sources is shown. Unlike the identifications carried out with FORS2 and EFOSC2, where almost all spectra down to $R \sim 24$ mag are useful (quality-flag $\geqslant$1.5), at R-band magnitudes fainter than $R \sim 19$ mag the fraction of low-quality VIMOS spectra increases with decreasing optical fluxes: it is about 20%, 35%, and 85% in the 21–22, 22–23, and 23–24 R-band magnitude bins, respectively. As a consequence, most (~80%) of the spectroscopic identifications at magnitudes fainter than $R = 23$ mag have been carried out only with FORS2, which is indeed much more efficient (because of better sky and fringe subtraction) at faint magnitudes. In the lower right panel of Figure 5, the R-band magnitude distribution of the fraction of each spectroscopic class among the good-quality spectra is shown.

The redshift histogram of the spectroscopically identified 24 μm sources and the 24 μm luminosity–redshift diagram are shown in Figure 6. The luminosities have been computed applying a K-correction derived by a best SED fitting (F. La Franca et al. 2010, in preparation): following Fiore et al. (2008) we used a modified version of the SED library described in Polletta et al. (2007) and already used for similar analyses by Lonsdale et al. (2004), Franceschini et al. (2005), Hatziminaoglou et al. (2005), Polletta et al. (2006), Weedman et al. (2006), and Tajer et al. (2007). The luminosity–redshift distribution is that typical of a flux-limited sample. On average, the most distant and luminous sources are the AGN1s, then there are the AGN2s, and finally the ELGs. As this is also an optical limited sample (the spectroscopic identifications reach $R \sim 24.2$ mag), the explanation of this behavior requires a proper analysis (which is beyond the scope of this paper) of the bivariate MIR/optical

luminosity functions of each population, combined with the *k*-corrections and all the selection effects. However, several works have been dedicated to the understanding of the shape of the 24 μm redshift distribution, discussing the combination of the effects of both the luminosity functions evolution and the MIR/optical SEDs (see, e.g., Pérez-González et al. 2005; Caputi et al. 2006; Desai et al. 2008). Desai et al. (2008) discuss in detail the redshift distribution of a sample of 591 24 μm sources, detected in the Boötes field of the NOAO Deep Wide-Field Survey, down to $F(24\ \mu\mathrm{m}) = 300\ \mu$Jy and spectroscopically identified down to $R = 25$ mag (thus with flux limits similar to our sample). They obtained optical spectroscopic redshift for 71% of the sources. Similarly to our sample, their redshift distribution shows a peak at $z \sim 0.3$ and a possible additional peak at $z \sim 0.9$ (see their Figure 9). These peaks could be attributed to redshifted emission features in the SED which enter the 24 μm MIPS bandpass. According to the analysis of Desai et al. (2008), the $z \sim 0.3$ peak is difficult to be reproduced, as only the polycyclic aromatic hydrocarbon (PAH) emission features at 16.3 and 17 μm can be partly responsible of its presence, while the $z \sim 0.9$ peak could be attributed to the 12.7 μm PAH feature and the 12.8 μm [Ne II] emission line passing trough the 24 μm bandpass. However, it is interesting to note that these two peaks are fairly well reproduced by the galaxy evolution model of Lagache et al. (2004; see Figure 11 in Desai et al. 2008) where both normal and starburst galaxies are represented by luminosity-dependent SEDs. The model encompasses a strong rate of evolution of the luminosity density of starburst galaxies, peaking at $z \sim 0.7$ and remaining constant up to $z = 4$, while the normal galaxies evolve up to $z = 0.4$, after which their luminosity density remains constant. Analyzing a fraction of their sources without emission-line redshifts, Desai et al. (2008) find also weak evidence for another peak at $z \sim 2$ where about 55% of the sources are AGN-dominated.

At redshift larger than 1.0, our distribution is populated by AGNs. AGN1s show larger redshifts and luminosities than AGN2s: 80% of the AGN1s have redshift larger than ∼0.9, while 80% of the AGN2s show redshift lower than ∼1.1. This redshift distribution is not unusual for an MIR sample combined to an optical flux limit (introduced by the spectroscopic identification and classification process). See, e.g., the luminosity–redshift distribution of the 15 μm selected ($F(15\ \mu\mathrm{m}) > 500\ \mu$Jy) sample in the whole ELAIS-S1 region by Matute et al. (2006; their Figure 3) where the spectroscopic identifications have been carried out down to $R \sim 22$ mag. In the 15 μm sample used by Matute et al. (2006), 90% of the AGN1s show redshift larger than ∼0.4, while 80% of the AGN2s have redshift lower than ∼0.4. The difference between the redshift distribution of the two AGN populations is due to a combination of their luminosity functions with a difference in the average MIR/Optical ratio of their SED. Although both AGN1s and (with larger uncertainties) AGN2s show a strong luminosity evolution in the MIR (e.g., Matute et al. 2006 find a luminosity evolution at 15 μm of $L(z) = L(0) \times (1+z)^k$ with $k \sim 2.9$ for AGN1 and $k \sim 1.8$–2.6 for AGN2; see also Brown et al. 2006 for a recent estimate of the AGN1 evolution at 24 μm), AGN2s have on average larger $F(24\ \mu\mathrm{m})/F(R)$ ratios than AGN1s (see, e.g., La Franca et al. (2004) and the discussion in Section 5.1.1 of this paper). In our sample, about 40% of the AGN2s show $F(24\ \mu\mathrm{m})/F(R)$ ratios larger than 100, while only 15% of the AGN1s have $F(24\ \mu\mathrm{m})/F(R)$ ratios larger than this limit. A similar kind of difference between AGN1 and AGN2 is seen in the X-rays, as far as the X-ray to optical ratio is concerned (see, e.g., Fiore et al. 2003). This happens because, in AGN2s, the optical AGN component is more often obscured, and the resulting optical spectrum is the combination of the hosting galaxy emission with the AGN Narrow Line Region (when visible; see, e.g., Fiore et al. 2000, 2003; Cocchia et al. 2007; and Caccianiga et al. 2008 for a discussion on the X-ray Bright Optically Normal Galaxies—XBONG). The average lower optical luminosity of AGN2s compared to the AGN1s (with the same 24 μm luminosity), combined to the optical $R = 24.2$ mag spectroscopic limit, is therefore one of the most important agent for the average lower redshifts of the AGN2 sample (the luminosity function and the *k*-corrections are the other most important ingredients). In summary, as the measure of the 24 μm AGN1 and AGN2 luminosity function is beyond the scope of this paper, we can comment that the similarity between the AGN1 and AGN2 luminosity–redshift distribution of our sample and that observed at 15 μm (Matute et al. 2006), suggests that it is qualitatively compatible with the previous estimates of the AGN evolution in the MIR (e.g., Matute et al. 2002, 2006; see also Brown et al. 2006), where all these selection effects have been taken into account.

4.2. The 3.6 μm Sample

Although the spectroscopic follow up was dedicated to the identification of the 24 μm and X-ray sources, a total of 1362 3.6 μm sources (881 not detected either in the 24 μm or the X-ray bands) have been spectroscopically identified. These spectra come from the identifications of 3.6 μm sources used as fillers of the VIMOS and FORS2 masks, or from the identification of the *K*-band (2.2 μm) sources of the western half area, observed during the first VIMOS run (see Section 3). We limit the following discussion to the western half of the VIMOS area having limits $8^{\circ}.21 < \alpha < 8^{\circ}.74$ and $-43^{\circ}.91 < \delta < -43^{\circ}.116$ that can be treated as an unbiased representation of the parent 3.6 μm sample and in which most of these sources (999) are indeed located (see Figure 1).

A total of 16,782 3.6 μm sources were detected by *Spitzer* within this 0.31 deg^2 area, 10,794 of which (64%) have been identified in the *R*-band optical ESIS catalog. Nine hundred and ninety nine sources have been spectroscopically identified: 762 result to be extragalactic sources and 237 stars. The extragalactic sources were classified into 111 AGNs (14.6%, 51 AGN1s and 60 AGN2s), 358 ELGs (47.0%), and 293 GALs (38.5%). Figure 7 shows the 3.6 μm flux histogram of the sub-sample (line on top), those with an *R*-band detection (hatched region) and those with a reliable redshift estimate (darker shaded area). The fraction of 3.6 μm sources with spectroscopic redshift is 22% for sources with $F(3.6\ \mu\mathrm{m}) > 50\ \mu$Jy and decreases at fainter fluxes (∼1% at $F(3.6\ \mu\mathrm{m}) \sim 30\ \mu$Jy).

In Figure 8, the distribution of the *R* magnitude as a function of the 3.6 μm flux is shown, with the indication of the spectroscopically identified and the X-ray detected sources. The fraction of spectroscopically identified sources decreases at both faint optical and 3.6 μm fluxes. Unlike the 24 μm sample, a decrease in the fraction of identifications is evident at bright optical and 3.6 μm fluxes too (see also Figure 7). This is due to the fact that the spectroscopic identifications of the sources brighter than $R = 18$ were carried out by single slit observations of the 24 μm sources only.

This bias is evident in the upper left panel of Figure 9 where the fraction of the 3.6 μm sources brighter than $R = 24$ which have been detected at 24 μm as a function of the 3.6 μm flux is shown. In the 3.6 μm flux interval between 10 and 160 μJy,

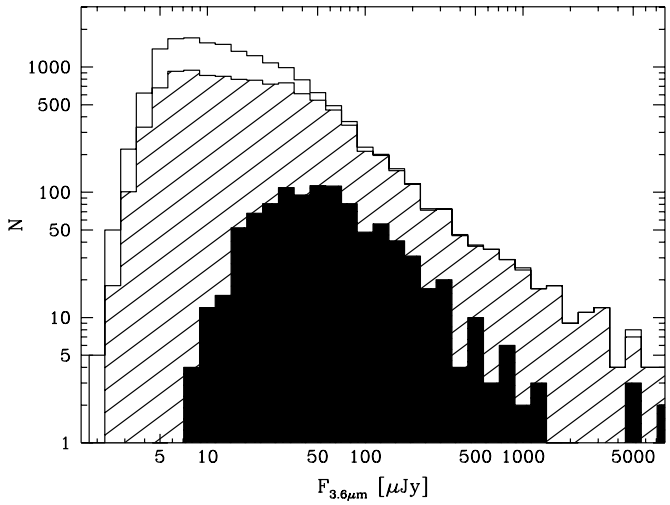

Figure 7. 3.6 μm flux distribution of all *Spitzer* sources (line on top), those with an *R*-band detection (hatched region), and those with a reliable redshift estimate (darker shaded area).

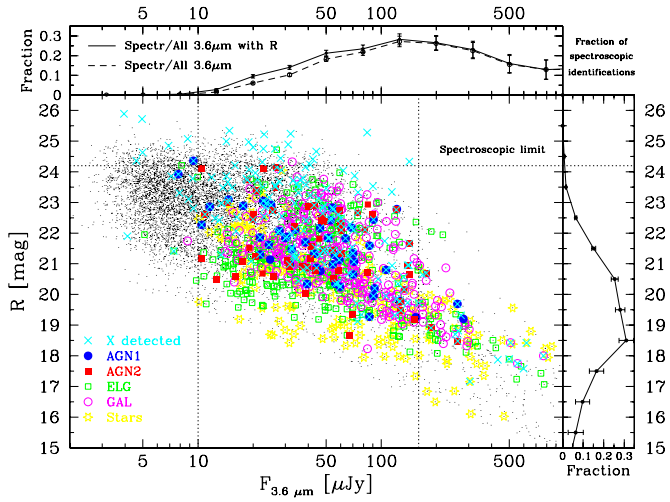

Figure 8. Central: *R* magnitude as a function of the 3.6 μm flux of the sources in the western half of the area. Those having a reliable redshift estimate are represented by symbols whose meaning is shown in the legend. Sources detected in the X-ray are indicated with cyan crosses. The two dotted vertical lines show the flux limits where, in each *R*-band magnitude interval, the spectroscopic identifications are a fair ("gray") sample of the 3.6 μm catalog (see Section 4.2). The horizontal dotted line represents the $R = 24.2$ mag limit of the spectroscopic identifications. Upper: fraction of the spectroscopically identified sources as a function of the 3.6 μm flux for the whole 3.6 μm sample (dashed line) and the *R*-band detected 3.6 μm sample (continuous line). Right: fraction of the spectroscopically identified 3.6 μm sources as a function of the *R*-band magnitude.

(A color version of this figure is available in the online journal.)

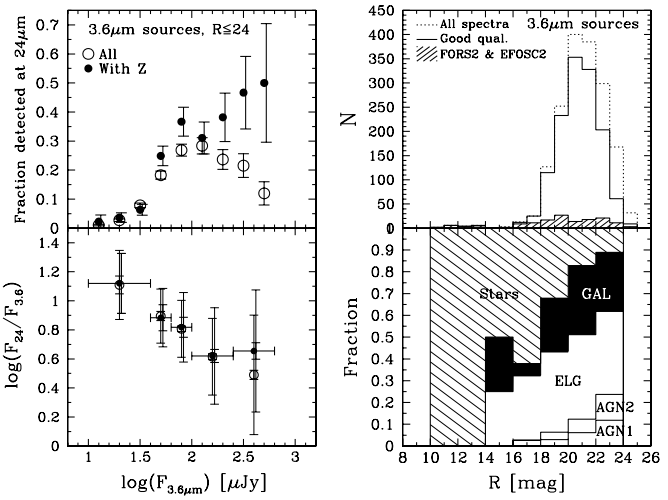

Figure 9. Upper left: fraction of the 3.6 μm sources brighter than $R = 24$ which have been detected at 24 μm as a function of the 3.6 μm flux. The whole sample and the spectroscopically identified one are represented by open and filled circles, respectively. Lower left: ratio of the 24 μm and 3.6 μm flux densities as a function of the 3.6 μm flux for the same samples. Symbols are as in the previous panel. Thick vertical error bars correspond to the (1σ) uncertainties on the mean, while the light vertical error bars show the (1σ) spread of the distributions. Upper right: *R* magnitude distribution of the spectroscopically observed 3.6 μm sources. The dotted line is the distribution of all the spectra, while the continuous line is the distribution of the "good quality" (qual $\geqslant$ 1.5) spectra presented in this work. The shaded area is the histogram of those sources whose spectra have been mainly obtained with FORS2/VLT (some of the brightest with EFOSC2/3.6 m or DFOSC). Lower right: fraction of the "good-quality" (qual $\geqslant$ 1.5) spectra of the 3.6 μm sources according to the spectroscopic class. Each histogram includes the classes below itself.

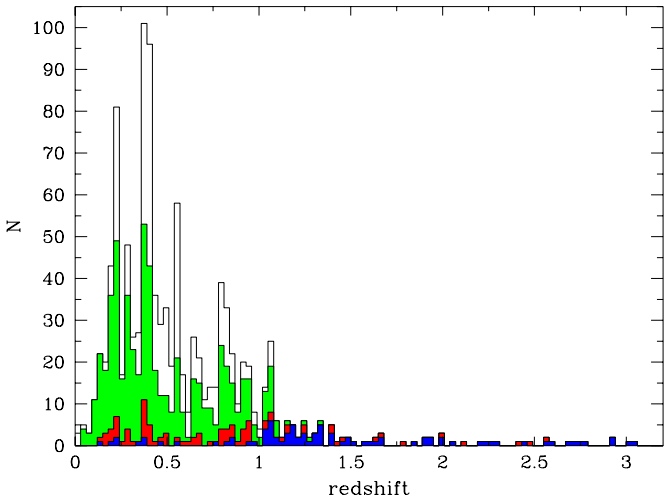

Figure 10. Redshift distribution of the 3.6 μm detected *Spitzer* sources. Those spectroscopically classified as AGN1, AGN2, and ELG are indicated in blue, red, and green colors, respectively (as in Figure 6).

(A color version of this figure is available in the online journal.)

there is no difference between the spectroscopic sample and the parent 3.6 μm sample. No difference is found either, in the same flux interval, between the $F(24\ \mu m)/F(3.6\ \mu m)$ ratios of the two samples (see the lower left panel in Figure 9). On the other hand, at 3.6 μm fluxes brighter than 160 μJy the fraction of 24 μm detected spectroscopically identified sources is significantly larger than the parent 3.6 μm sample. We can then conclude that, within the western half of the area, in each *R*-band magnitude interval brighter than $R \sim 24$, the 3.6 μm spectroscopic catalog is a fair sample of the 3.6 μm sources only in the 10–160 μJy flux range.

In the upper right panel of Figure 9 the *R*-band distribution of the spectroscopically identified 3.6 μm sources is shown, while in the lower right panel of Figure 9 the *R*-band magnitude distribution of the fraction of each spectroscopic class among the good-quality spectra is shown. Unlike the spectroscopic 24 μm sample (see Figure 5 for comparison) even at faint *R*-band magnitudes ($R \sim$ 22–24), a large fraction (about 40%) of the sources are non-emission line galaxies (GALs) and stars. The redshift histogram of the spectroscopically identified 3.6 μm sources is shown in Figure 10.

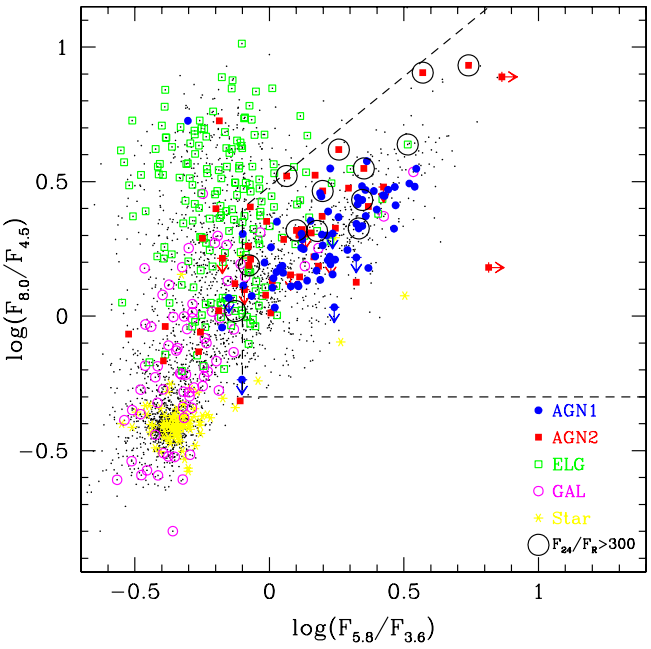

Figure 11. IRAC color–color diagram of the spectroscopically classified 3.6 μm sources. Black points show all the sources detected in all the four IRAC bands. The dashed line shows the AGN selection criteria proposed by Lacy et al. (2004, 2007). Open black circles indicate those 24 μm sources having $F(24\ \mu\mathrm{m})/F(R)$ ratios larger than 300. For more information about the sources distribution, see, e.g., Sajina et al. (2005).

(A color version of this figure is available in the online journal.)

4.2.1. IRAC Colors

With the launch of *Spitzer*, some color–color diagrams (mainly based on the IRAC photometry) have been proposed in order to quickly characterize the MIR SED properties of the sources and select the AGN (see, e.g., Lacy et al. 2004; Stern et al. 2005; Lacy et al. 2007). In Figure 11, the IRAC color–color diagram, as proposed by Lacy et al. (2004, 2007), of all the spectroscopically classified 3.6 μm sources is shown. The dashed line shows the original AGN selection criteria, calibrated on a Sloan Digital Sky Survey quasar sample and subsequently confirmed with spectroscopic observations. The study of the relations among the average SED properties of the sources and their optical spectra is beyond the scope of this paper. However, we can note that, as in the above mentioned studies, also the sources of our sample occupy two branches, forming a "V"-shaped locus. Each spectroscopic class preferentially occupies different regions of the diagram according to the energetically dominant component in the MIR regime (see, e.g., Sajina et al. 2005). In line with the above-mentioned studies, ∼85% of the AGNs (97% of the AGN1s and 70% of the AGN2s detected in all the four IRAC bands) in our sample are located inside the AGN selection region (the branch on the right) corresponding to sources having red power-law MIR-SEDs whose slope increases moving to the upper right part of the diagram. ELGs and GALs occupy (without solution of continuity) the upper and lower region, respectively, of the left branch. Stars are located at the bottom, almost in the center of the passive galaxy locus, as they have qualitatively similar SEDs (with an emission shortfall in the MIR).

5. FRACTION OF AGN

As discussed in the introduction, it is very interesting to measure the fraction of AGNs among those sources showing large $F(24\ \mu\mathrm{m})/F(R)$ ratios or as a function of the 24 μm flux. In order to use the most statistically useful sample, in the following analyses we will use the sub-sample of the spectroscopic catalog of the 24 μm extragalactic sources corresponding to the intersection of the area of the spectroscopic follow up (see Section 4.1) with the area covered by the *XMM-Newton* observations (see also Figure 1). As discussed in Section 4.1, we select a sub-sample at 24 μm fluxes brighter than 280 μJy and magnitudes brighter than $R = 24.2$, which corresponds to the largest possible sample where sufficient spectroscopic information exists. These selections correspond to an area of 0.54 deg^2.

5.1. Fraction of AGNs as a Function of the $F(24\ \mu\mathrm{m})/F(R)$ Ratio

The spectroscopic campaign has been carried out observing sources detected by either *XMM-Newton* or *Spitzer* (or both). Eighty three of the 419 spectroscopically identified 24 μm sources are also included in the *XMM-Newton* detection catalog (see Table 1). Therefore, in the estimate of the AGN fraction as a function of the $F(24\ \mu\mathrm{m})/F(R)$ ratio, a correction for the bias introduced by the inclusion of the X-ray sample has to be taken into account (indeed, as shown by Feruglio et al. (2008), most of the X-ray sources are AGN). If we call N_{X} (and $N_{\mathrm{X,spec}}$) and N_{NoX} (and $N_{\mathrm{NoX,spec}}$) the number of *Spitzer* sources (and those spectroscopically identified) in a given MIR flux interval, detected and not detected in the X-ray band, respectively, the true fraction of AGN ($\mathrm{Fr}_{\mathrm{AGN}}$) among all ($N_{\mathrm{Tot}}$) the *Spitzer* sources is given by

$$\mathrm{Fr}_{\mathrm{AGN}} = \left(\frac{N_{\mathrm{X,AGN}}}{N_{\mathrm{X,spec}}}N_{\mathrm{X}} + \frac{N_{\mathrm{NoX,AGN}}}{N_{\mathrm{NoX,spec}}}N_{\mathrm{NoX}}\right) \Big/ N_{\mathrm{Tot}},$$

where $N_{\mathrm{X,AGN}}$ and $N_{\mathrm{NoX,AGN}}$ are the number of spectroscopically identified AGN, detected and not detected in the X-ray band, respectively.

We have verified that, although the fraction of spectroscopic identifications decreases at faint R-band magnitudes, in each $F(24\ \mu\mathrm{m})/F(R)$ bin the fraction of spectroscopic identifications is not significantly dependent on either the 24 μm flux or the R-band magnitude (see Figure 12). Therefore, the spectroscopic identifications provide a fair random sampling of the sources in each $F(24\ \mu\mathrm{m})/F(R)$ bin.

The fraction of AGN as a function of the $F(24\ \mu\mathrm{m})/F(R)$ ratio is shown in Figure 13, while in Figure 14 the redshift of the spectroscopically identified sources as a function of the $F(24\ \mu\mathrm{m})/F(R)$ ratio is plotted. The fraction of AGN clearly increases with increasing $F(24\ \mu\mathrm{m})/F(R)$ ratio. While 85% of the AGN1 concentrates in the range $1 < \log[F(24\ \mu\mathrm{m})/F(R)] < 2$, which is typical of the local AGN1 SEDs (e.g., Spinoglio et al. 2002), the AGN2 fraction constantly increases with the $F(24\ \mu\mathrm{m})/F(R)$ ratio: in the $2.5 < \log[F(24\ \mu\mathrm{m})/F(R)] < 3$ interval (where a total of 18 sources have been spectroscopically identified) AGN2 outnumber AGN1 by a factor of ∼5, and the total fraction of AGN is 70(±20)%.

However, it should be noted that this statistics could be affected by some biases. In poor-quality data, emission line spectra are more easily identified than no-emission line spectra. In the $2.5 < \log[F(24\ \mu\mathrm{m})/F(R)] < 3$ interval, beside the 18 classified spectra, eight further FORS2 spectra (with similar R-band distribution) missed an identification. These additional eight spectra could be populated by the same mixture of AGN1s, AGN2s, ELGs, and passive galaxies, but, under the

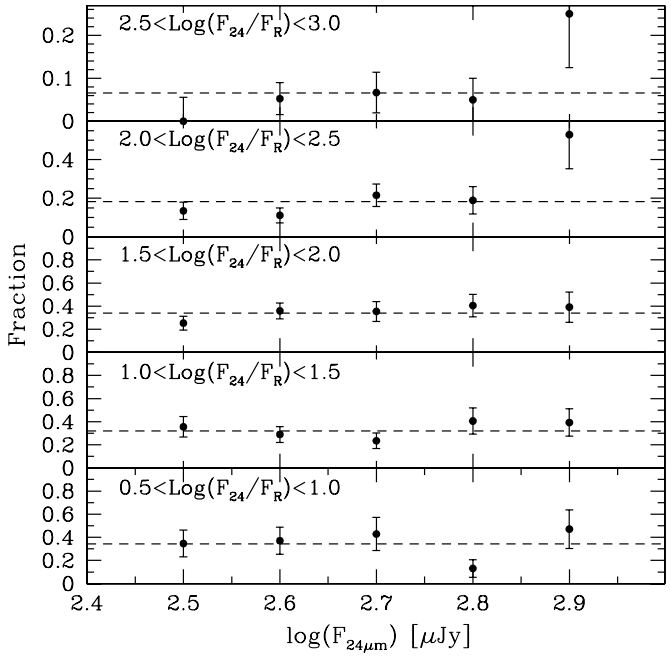

Figure 12. Fraction of spectroscopically identified 24 μm sources as a function of the $F(24\ \mu\mathrm{m})$ flux divided into different bins of the $F(24\ \mu\mathrm{m})/F(R)$ ratio (the dashed horizontal lines indicate mean values in each $F(24\ \mu\mathrm{m})/F(R)$ bin). Given the narrow dimension of the intervals in $F(24\ \mu\mathrm{m})/F(R)$, the overall constant trend in $F(24\ \mu\mathrm{m})$ is similar in $F(R)$ as well.

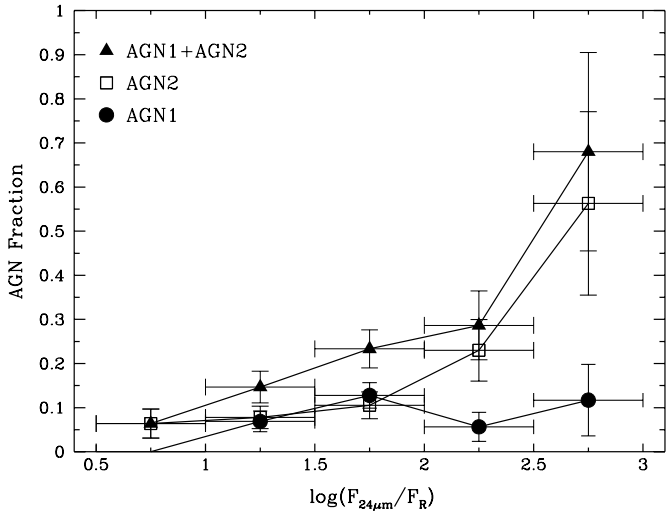

Figure 13. Fraction of AGNs as a function of the $F(24\ \mu\mathrm{m})/F(R)$ ratio (triangles). Filled circles represent the fraction of AGN1s, while open squares represent the fraction of AGN2s. Horizontal error bars represent the ratio interval; vertical bars represent the Poissonian errors propagated through the $\mathrm{Fr_{AGN}}$ formula in Section 5.1.

most extreme assumption that all these objects were included among the non-AGN sample, the fraction of AGNs in the $2.5 < \log[F(24\ \mu\mathrm{m})/F(R)] < 3$ interval would be 50%, instead of 70%. Therefore, although our estimate of a fraction of 70% AGN in the $2.5 < \log[F(24\ \mu\mathrm{m})/F(R)] < 3$ interval has not to be considered an upper limit, it should be bear in mind that if this bias were present, the real dependence of the AGNs fraction with increasing $F(24\ \mu\mathrm{m})/F(R)$ ratio would be weaker (but still present) than shown in Figure 13.

On the other hand, in Section 3.5, we have stated that a fraction (which is difficult to quantify) of the ELG classified sources could instead be AGN2s if identified with higher S/N optical spectra. Although we are not able to quantify this bias,

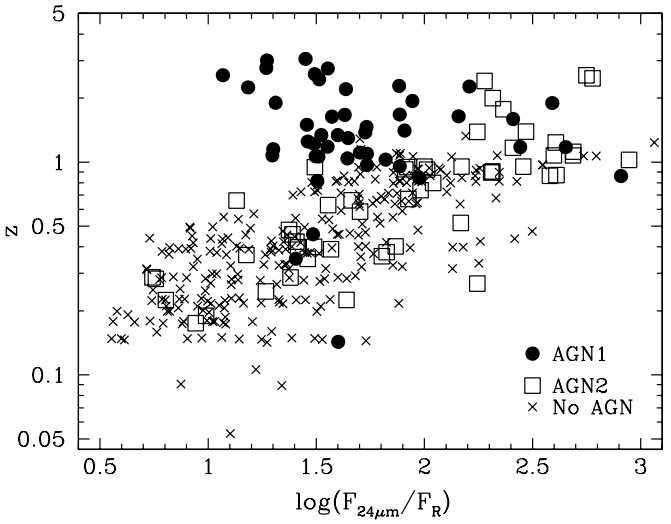

Figure 14. Redshift of the spectroscopically identified sources as a function of the $F(24\ \mu\mathrm{m})/F(R)$ ratio. Filled circles and open squares represent AGN1s and AGN2s, respectively.

we can qualitatively expect it to be more relevant for the optically fainter sources, whose $F(24\ \mu\mathrm{m})/F(R)$ ratio is on average larger. In this case, the increase of the AGN fraction with increasing $F(24\ \mu\mathrm{m})/F(R)$ ratio would be even more relevant.

In Figure 15, the optical spectra of the 18 sources with $2.5 < \log[F(24\ \mu\mathrm{m})/F(R)] < 3$ are shown. The positions of typical AGN emission lines (even if not observed) are shown as a reference. Ten out of the 14 spectra with magnitudes larger than $R = 22.5$ mag have been observed by FORS2. The AGN2s show larger [O III] λ5007/Hβ and [O II] λ3727/Hβ ratios than observed in the ELG, typical of AGN activity (e.g., Osterbrock 1989). Moreover, when observable, AGN2s show the high-ionization [Ne V] λ3426 emission line, which instead is not present in the ELG spectra (see also Figure 2).

The observed differences on the $F(24\ \mu\mathrm{m})/F(R)$ ratios of AGN1s and AGN2s is principally explained by the difference between their optical luminosity. While in AGN1s the optical luminosity originates directly in the nucleus, in AGN2s, as the AGN is obscured, the optical luminosity comes from the lower luminous hosting galaxy. As shown in Figures 6 and 14, for non-AGN1 sources the average redshift increases with increasing $F(24\ \mu\mathrm{m})/F(R)$ ratio. All the sources with $\log[F(24\ \mu\mathrm{m})/F(R)] > 2.5$ have $z > 0.8$, and νL_ν 24 μm luminosity larger than 10^{44} erg s^{-1}. This behavior is due to the fact that those non-AGN1 sources showing larger $F(24\ \mu\mathrm{m})/F(R)$ ratio have preferentially the faintest optical magnitudes and thus the largest redshift. In contrast, AGN1 are more easily found at large redshifts but with lower (roughly constant) $F(24\ \mu\mathrm{m})/F(R)$ ratios. In this case (as discussed in Section 4.1), this is caused by the evolution of AGN1 luminosity functions (the density increases with increasing redshift[19]) combined with the accessible volumes and k-corrections (see, e.g., Matute et al. 2002, 2006), while the average SED (and then the $F(24\ \mu\mathrm{m})/F(R)$ ratio) does not evolve significantly.

5.1.1. IRAC–MIPS Color–Color Selection of Absorbed AGN

As shown in Figure 11, the sources with large (>300) $F(24\ \mu\mathrm{m})/F(R)$ ratios are mostly located in the IRAC color–color

[19] A luminosity evolution results in an increase of the density of sources with the same luminosity.

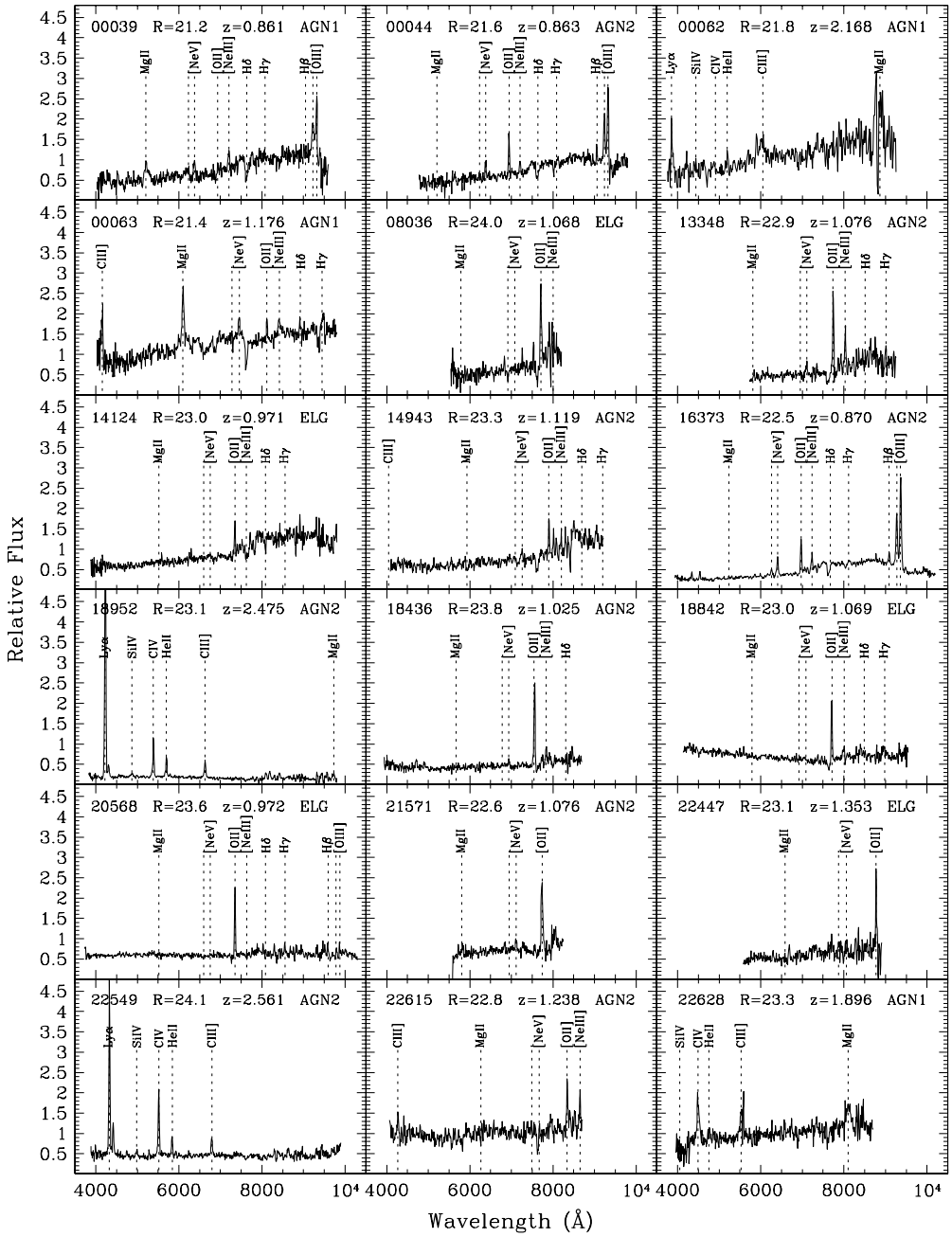

Figure 15. Optical spectra of the 18 sources with $2.5 < \log(F(24\ \mu\mathrm{m})/F(R)) < 3$. The positions of typical AGN emission lines (even if not observed) are shown as a reference.

region where AGNs are expected: i.e., in the branch where both the $F(5.8\ \mu\mathrm{m})/F(3.6\ \mu\mathrm{m})$ and $F(8.0\ \mu\mathrm{m})/F(4.5\ \mu\mathrm{m})$ ratios are larger. However, it is evident that the $F(5.8\ \mu\mathrm{m})/F(3.6\ \mu\mathrm{m})$ ratio is more efficient than the $F(8.0\ \mu\mathrm{m})/F(4.5\ \mu\mathrm{m})$ ratio in the AGN selection. It is therefore possible to create an optical–IRAC–MIPS color–color diagram, based on the $F(5.8\ \mu\mathrm{m})/F(3.6\ \mu\mathrm{m})$ and $F(24\ \mu\mathrm{m})/F(R)$ ratios, which is highly efficient in selecting obscured AGNs (AGN2s).

Figure 16 shows how this optical–IRAC–MIPS diagram is populated according to our spectroscopic classification. The region with $\log[F(5.8\ \mu\mathrm{m})/F(3.6\ \mu\mathrm{m})] > 0$ and $1 < \log[F(24\ \mu\mathrm{m})/F(R)] < 2$ is mainly populated by AGN1s: 65% are AGN1s and 12% are AGN2s (79% of all the AGN1s are located in this region). The region with $\log[F(5.8\ \mu\mathrm{m})/F(3.6\ \mu\mathrm{m})] > 0$ and $\log[F(24\ \mu\mathrm{m})/F(R)] > 2$ is mainly populated by AGN2s: 24% are AGN1s and 55% are AGN2s (36% of all the AGN2s are included in this area). Therefore, while the first region is quite efficient in selecting AGN1s, the second one is useful in selecting obscured AGN2s with a moderate level of completeness.

5.2. Fraction of AGNs as a Function of the 24 μm Flux

The measure of the fraction (and counts) of AGNs as a function of the 24 μm flux is a very useful information to constrain the evolutionary models of AGNs and starburst galaxies (see, e.g., Gruppioni et al. 2005; Franceschini et al. 2008). Unlike for the estimate of the AGN fraction as a function of the $F(24\ \mu\mathrm{m})/F(R)$ ratio (presented in the previous section), in this case, the presence in our sample of a decrease of the

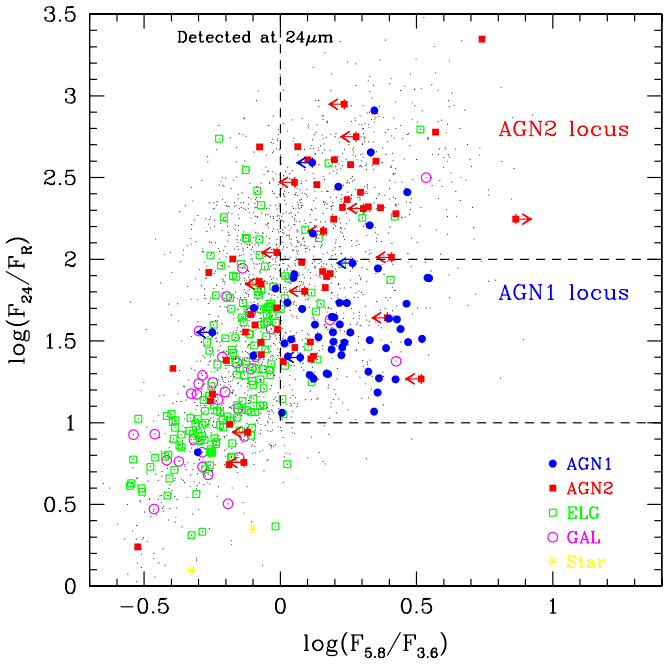

Figure 16. $F(24\ \mu m)/F(R)$ ratio as a function of the (IRAC) $F(5.8\ \mu m)/F(3.6\ \mu m)$ ratio of 24 μm detected sources. The loci mostly populated by AGN1s and obscured AGN2s are delimited by dashed lines (the respective fractions are reported in the text). The larger $F(24\ \mu m)/F(R)$ ratio of AGN2s compared to AGN1s is due to the stronger obscuration in the optical for AGN2s, while the $F(5.8\ \mu m)/F(3.6\ \mu m)$ separation between ELGs and AGNs is mainly due to the PAH features present in most IR galaxies combined with a redshift effect (for more information, see, e.g., Sajina et al. 2005). The classification of the spectroscopically identified sources is shown in the legend.

(A color version of this figure is available in the online journal.)

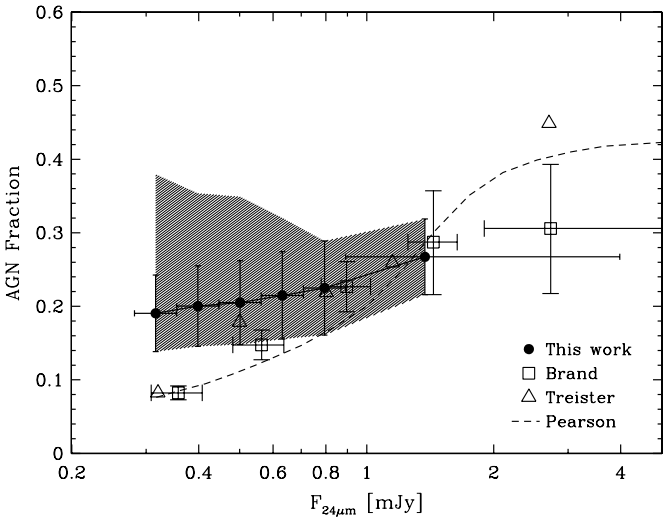

Figure 17. Fraction of optically classified AGNs as a function of the 24 μm flux. The shaded area shows the 1σ confidence limits once the sources not detected in the R band are included and assumed to contain a fraction of 68% of AGNs, as measured in the $2.5 < \log[F(24\ \mu m)/F(R)] < 3$ bin. Overplotted are the estimates based on both X-ray and *Spitzer* data from Brand et al. (2006; squares) and Treister et al. (2006; triangles). The dashed line shows the expectations from the burst model of Pearson (2005). Horizontal error bars of our data represent the flux interval.

fraction of spectroscopically identified sources with decreasing R-band magnitudes (see Figure 4) and, on top of that, the lack of any identification at magnitudes fainter than $R = 24.2$, complicates the attainment of a reliable measure.

In order to overcome these difficulties, and still obtain a sufficiently useful estimate, we have derived the fraction of AGNs as a function of the 24 μm flux by assuming that it is mainly dependent on the $F(24\ \mu m)/F(R)$ ratio as measured in the previous section. The AGN fraction was then derived by dividing each 24 μm flux interval into $F(24\ \mu m)/F(R)$ bins and multiplying the number of sources in each bin to its previously measured fraction of AGNs (see Figure 13).

In Figure 17, the corresponding fraction of optically classified AGNs as a function of the 24 μm flux is shown. The shaded area corresponds to the 1σ confidence limits once the sources not detected in the R band are also included and assumed to contain a fraction of 68% of AGNs, as measured for the objects with the largest $F(24\ \mu m)/F(R)$ ratio. The AGN fraction at $F(24\ \mu m) \sim 0.8$ mJy results to be $\sim 22(\pm 7)\%$ and decreases slowly to $\sim 19(\pm 5)\%$ down to $F(24\ \mu m) \sim 0.3$ mJy. This estimate of the fraction of optically classified AGNs, at 24 μm fluxes fainter than 0.8 mJy, is larger than the previous measures by Brand et al. (2006) and Treister et al. (2006) and the expectations of the burst model of Pearson (2005; see Figure 17). It should be noted that our measure of the AGN fraction is based on a direct spectroscopic optical classification, while the estimates from Brand et al. (2006) are based on a classification which uses *Spitzer* colors (selecting sources in which the MIR emission is AGN dominated), and Treister et al. (2006) use a selection in the hard-X band and then corrects by the absorbed AGN fraction expected to be missed assuming an N_H population distribution.

The real fraction of AGNs would be even larger if we took into account that a fraction ($\sim$10%) of X-ray (or even MIR) classified AGNs do not show in the optical signatures of AGN activity (e.g., the XBONG; see Fiore et al. 2000, 2003; La Franca et al. 2007; Cocchia et al. 2007; Caccianiga et al. 2008; Gruppioni et al. 2008; Feruglio et al. 2008 and references therein). These objects usually show large values of both X-ray to optical and MIR to optical flux ratios.

6. DISCUSSION AND CONCLUSIONS

As discussed in the introduction, several studies have presented evidence that many galaxies showing SEDs with large $F(24\ \mu m)/F(R)$ ratios (e.g., Polletta et al. 2008 use a threshold of $F(24\ \mu m)/F(R) > 400$ and 24 μm fluxes larger than 1 mJy) harbor an AGN. These works were mainly based on low-resolution MIR spectroscopy or SED studies. X-ray stacking analyses of sources with $F(24\ \mu m)/F(R) > 1000$ have shown that their *average* X-ray spectrum is compatible with Compton-thin and Compton-thick absorbed sources (Daddi et al. 2007; Fiore et al. 2008, 2009), but the relevance of this result depends on the fraction of AGNs (and complementary starburst galaxies) which contribute to the average X-ray spectrum (see Donley et al. 2008).

Our catalog of 1376 optical spectroscopic identifications of 3.6 and 24 μm SWIRE sources, thanks to the use of FORS2 and VIMOS at VLT, has pushed the optical classification down to $R \sim 24$, and has allowed us to directly measure the fraction of AGNs as a function of the $F(24\ \mu m)/F(R)$ ratio. We have then shown that, at 24 μm fluxes larger than 280 μJy, in the range $316 < F(24\ \mu m)/F(R) < 1000$, $70(\pm 20)\%$ of the sources show an optical AGN spectrum, and most of them are AGN2s. In fact, the increase of the total fraction of AGNs with the $F(24\ \mu m)/F(R)$ ratio is caused by a strong increase of the fraction of AGN2s, which populate more than 80% of the AGNs found in the $316 < F(24\ \mu m)/F(R) < 1000$ range. This result is in agreement with the above-mentioned observed average X-ray

absorbed spectrum reported for similar kind of sources. Indeed, in the framework of the classical unified AGN scenario X-ray absorbed spectra are typical of AGN2s.

At fainter optical luminosity ($R > 24$) and then larger $F(24\ \mu\mathrm{m})/F(R)$ ratios the fraction of AGNs might be even higher, but the optical spectroscopic identification of a statistical significant sample of these sources is difficult to achieve with the currently available 8 m class telescopes.

Our result confirms previous indications that the population of sources showing large $F(24\ \mu\mathrm{m})/F(R)$ ratios are mainly AGN2s (e.g., Daddi et al. 2007; Fiore et al. 2008, 2009), but as we were able to spectroscopically separate the AGN(2)s from the starburst galaxies, we are now able to measure how many and how much of these AGNs show X-ray absorption and, even more interestingly, if they include a significant fraction of the long searched and predicted Compton-thick AGN population. Such a kind of study requires the use of deep *Chandra* X-ray observations which, in ELAIS-S1, partly already exist (S. Puccetti et al. 2010, in preparation), and will be the subject of a forthcoming paper.

Based on observations made with the ESO telescopes at the La Silla and Paranal Observatories under program IDs 168.A-0322, 170.A-0143, 073.A-0446, 075.A-0428, 076.A-0225, 077.A-0800, and 078.A-0795. Part of the data published in this paper have been reduced using VIPGI, designed by the VIRMOS Consortium and developed by INAF Milano. We are grateful to Bianca Garilli and Marco Scodeggio for the support provided in running the VIPGI pipeline. This work is based on observations made with the *Spitzer Space Telescope*, which is operated by the Jet Propulsion Laboratory, California Institute of Technology under a contract with NASA. We acknowledge financial contribution from contract ASI-INAF I/023/05/0, PRIN-MIUR grant 2006-02-5203. The anonymous referee is acknowledged for his detailed and constructive reports.

Facilities: VLT:Melipal (VIMOS), VLT:Antu (FORS2), ESO:3.6 m (EFOSC2), *Spitzer*

REFERENCES

Alexander, D. M., et al. 2001, ApJ, 554, 18
Alexander, D. M., et al. 2008, ApJ, 687, 835
Alonso-Herrero, A., et al. 2006, ApJ, 640, 167
Ballantyne, D. R., Shi, Y., Rieke, G. H., Donley, J. L., Papovich, C., & Rigby, J. R. 2006, ApJ, 653, 1070
Berta, S., et al. 2006, A&A, 451, 881
Berta, S., et al. 2008, A&A, 488, 533
Brand, K., et al. 2006, ApJ, 644, 143
Brand, K., et al. 2007, ApJ, 663, 204
Brand, K., et al. 2008, ApJ, 680, 119
Brown, M. J. I., et al. 2006, ApJ, 638, 88
Burgarella, D., et al. 2005, ApJ, 619, L63
Caccianiga, A., et al. 2008, A&A, 477, 735
Caputi, K. I., et al. 2006, ApJ, 637, 727
Cocchia, F., et al. 2007, A&A, 466, 31
Daddi, E., et al. 2007, ApJ, 670, 173
Davis, M., et al. 2007, ApJ, 660, L1
Desai, V., et al. 2008, ApJ, 679, 1204
Dey, A., et al. 2008, ApJ, 677, 943
Donley, J. L., Rieke, G. H., Pérez-González, P. G., & Barro, 2008, ApJ, 687, 111
Donley, J. L., Rieke, G. H., Pérez-González, P. G., Rigby, J. R., & Alonso-Herrero, A. 2007, ApJ, 660, 167
Donley, J. L., et al. 2005, AJ, 129, 220
Fadda, D., et al. 2006, AJ, 131, 2859
Fazio, G. G., et al. 2004, ApJS, 154, 10
Feruglio, C., et al. 2008, A&A, 488, 417
Fiore, F., et al. 2000, New Astron., 5, 143
Fiore, F., et al. 2003, A&A, 409, 79
Fiore, F., et al. 2008, ApJ, 672, 94
Fiore, F., et al. 2009, ApJ, 693, 447
Franceschini, A., et al. 2005, AJ, 129, 2074
Franceschini, A., et al. 2008, A&A, 487, 837
Gruppioni, C., Pozzi, F., Lari, C., Oliver, S., & Rodighiero, G. 2005, ApJ, 618, L9
Gruppioni, C., et al. 1999, MNRAS, 305, 297
Gruppioni, C., et al. 2008, ApJ, 684, 136
Hasinger, G. 2008, A&A, 490, 905
Hatziminaoglou, E., et al. 2005, AJ, 129, 1198
Houck, J. R., et al. 2005, ApJ, 622, L105
Kewley, L. J., et al. 2006, MNRAS, 372, 961
Lacy, M., Petric, A. O., Sajina, A., Canalizo, G., Storrie-Lombardi, L. J., Armus, L., Fadda, D., & Marleau, F. R. 2007, AJ, 133, 186
Lacy, M., et al. 2004, ApJS, 154, 166
La Franca, F., et al. 2004, AJ, 127, 3075
La Franca, F., et al. 2005, ApJ, 635, 864
La Franca, F., et al. 2007, A&A, 472, 797
Lagache, G., et al. 2004, ApJS, 154, 112
Lari, C., et al. 2001, MNRAS, 325, 1173
Lawrence, A., & Elvis, M. 1982, ApJ, 256, 410
Lonsdale, C. J., et al. 2003, PASP, 115, 897
Lonsdale, C. J., et al. 2004, ApJS, 154, 54
Martínez-Sansigre, A., Rawlings, S., Lacy, M., Fadda, D., Marleau, F. R., Simpson, C., Willott, C. J., & Jarvis, M. J. 2005, Nature, 436, 666
Martínez-Sansigre, A., et al. 2007, MNRAS, 379, L6
Matute, I., La Franca, F., Pozzi, F., Gruppioni, C., Lari, C., & Zamorani, G. 2006, A&A, 451, 443
Matute, I., et al. 2002, MNRAS, 332, L11
Middelberg, E., et al. 2008, AJ, 135, 1276
Murray, S. S., et al. 2005, ApJS, 161, 1
Oliver, S., et al. 2000, MNRAS, 316, 749
Osterbrock, D. E. 1989, Astrophysics of Gaseous Nebulae and Active Galactic Nuclei (Mill Valley, CA: Univ. Science Books)
Pearson, C. 2005, MNRAS, 358, 1417
Pérez-González, P. G., et al. 2005, ApJ, 630, 82
Polletta, M., Weedman, D., Hönig, S., Lonsdale, C. J., Smith, H. E., & Houck, J. 2008, ApJ, 675, 960
Polletta, M., et al. 2006, ApJ, 642, 673
Polletta, M., et al. 2007, ApJ, 663, 81
Pope, A., et al. 2008, ApJ, 689, 127
Puccetti, S., et al. 2006, A&A, 457, 501
Rieke, G. H., et al. 2004, ApJS, 154, 25
Rowan-Robinson, M., et al. 2004, MNRAS, 351, 1290
Sajina, A., et al. 2005, ApJ, 621, 256
Scodeggio, M., et al. 2005, PASP, 117, 1284
Spinoglio, L., Andreani, P., & Malkan, M. A. 2002, ApJ, 572, 105
Steffen, A. T., Brandt, W. N., Alexander, D. M., Gallagher, S. C., & Lehmer, B. D. 2007, ApJ, 667, L25
Stern, D., et al. 2005, ApJ, 631, 163
Surace, J. A., Shupe, D. L., Fang, F., Evans, T., Alexov, A., Frayer, D., Lonsdale, C. J., & SWIRE Team 2005, BAAS, 37, 1246
Tajer, M., et al. 2007, A&A, 467, 73
Treister, E., & Urry, C. M. 2006, ApJ, 652, L79
Treister, E., et al. 2006, ApJ, 640, 603
Treister, E., et al. 2009, ApJ, 693, 1713
Tresse, L., et al. 1996, MNRAS, 281, 847
Ueda, Y., Akiyama, M., Ohta, K., & Miyaji, T. 2003, ApJ, 598, 886
Veilleux, S., & Osterbrock, D. E. 1987, ApJS, 63, 295
Weedman, D. W., et al. 2006, ApJ, 651, 101
Yan, L., et al. 2007, ApJ, 658, 778